

# Periodically poled thin-film lithium niobate microring resonators with a second-harmonic generation efficiency of 250,000 %/W: supplementary material

JUANJUAN LU, JOSHUA B. SURYA, XIANWEN LIU, ALEXANDER W. BRUCH, ZHENG GONG, YUNTAO XU, AND HONG X. TANG\*

Department of Electrical Engineering, Yale University, New Haven, Connecticut 06511, USA

\*Corresponding author: hong.tang@yale.edu

Published November 21, 2019

This document provides supplementary information to “Periodically poled thin-film lithium niobate microring resonators with a second-harmonic generation efficiency of 250,000 %/W,” <https://doi.org/10.1364/OPTICA.6.001455>.

## 1. BARE Z-CUT LNOI WAFER POLING PROCESS AND DOMAIN CHARACTERIZATION

The undoped congruent thin film lithium niobate on insulator (LNOI) wafer (supplied by NANOLN) consists of three layers. They are the z-cut lithium niobate (LN) thin film (600 nm, spontaneous polarization along the z axis perpendicular to the sample surface), SiO<sub>2</sub> (1.9 μm), and silicon substrate (400 μm), from top to bottom. To test the poling process, a bare z-cut LNOI wafer was used. First, a 100 nm thick nickel was deposited on top of the LN layer by electron beam evaporation after defining the radial grating pattern using electron-beam lithography. Then, the sample was placed on an aluminum plate, which acted as the ground electrode and was heated to an elevated temperature of 250 °C. Six voltage pulses with amplitude of 600 V and width of 250 ms were applied to the nickel electrodes to enable the domain inversion. The poling setup and pulse shape are shown in Fig. 2 of the main text.

After the poling process, the regions covered by the electrodes were supposed to exhibit inverted crystal domains while the uncovered region remained unchanged. We first utilized piezoresponse force microscopy (PFM) to visualize the domain inversion after removing the nickel electrodes in hydrochloric acid as shown in Figs. S1(a-b). Traces of nickel patterns were slightly visible from the acquired topography (Fig. S1(a)), probably due to different surface properties between the covered and uncovered regime by the nickel electrodes. Periodic ferroelectric domain structure was best verified from the phase image (Fig. S1(b)), where the dark regions correspond to the inverted domains. Lateral domain spreading under the electrodes was apparent and resolved by designing electrodes with smaller duty

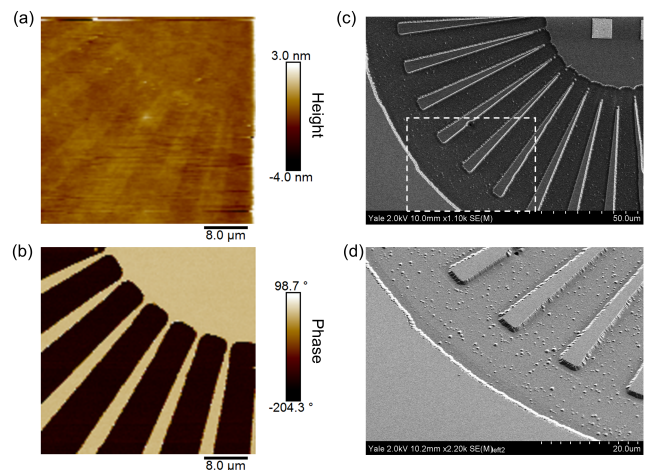
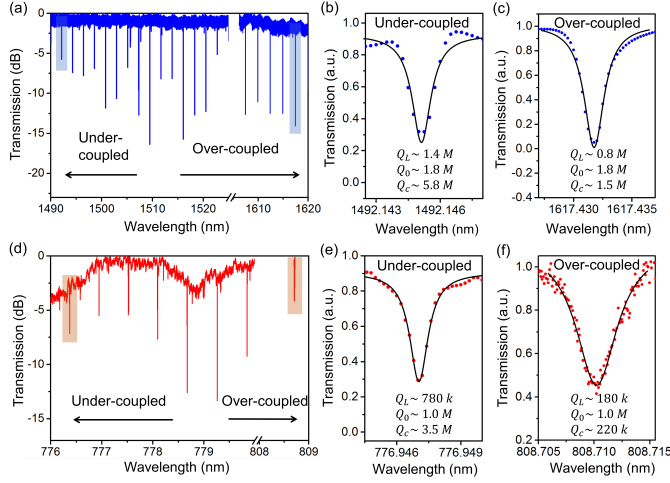


**Fig. S1.** (a-b) PFM images of periodically poled thin film z-cut LNOI showing simultaneously the topography (a) and ferroelectric domain structure (b). (c-d) SEM images of a periodically poled z-cut LNOI chip after submerging it in HF, revealing a radial grating pattern with the inverted domain selectively etched down.

cycle than the targeted value of 50% during the poling process of LN microrings. Finally, the difference in etch rates between the poled and unpoled regions of z-cut LN in hydrofluoric acid (HF) [1] allowed us to examine the poling quality under a scanning electron microscope (SEM). As shown in Figs. S1(c-d), while the domain structures are mostly defined by the electrodes, the

residues on top of the etched poled region indicate remnant inhomogeneity of the inverted domain. Additionally, imperfections of the poling as observed from the tilted domain sidewalls and deviations of domain boundaries could give rise to a suppressed  $\chi_{\text{eff}}^{(2)}$  coefficient, and thereby compromise the resulting second-harmonic generation (SHG) efficiency  $\eta$  in the periodically poled lithium niobate (PPLN) microring devices.

## 2. OPTICAL Q-FACTOR MEASUREMENT



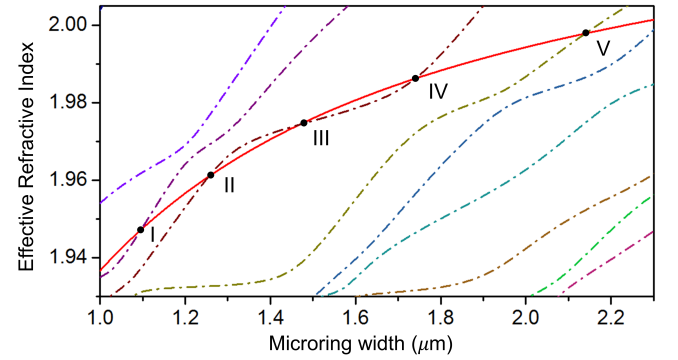
**Fig. S2.** (a) Transmission spectrum of the PPLN microring in the telecom band, showing a clear evolution of the extinction ratios of the resonances as the pump wavelength increased, with the highest extinction seen around 1510 nm. (b) An under-coupled resonance around 1492.1 nm with extracted Q factors. (c) An over-coupled resonance around 1617.4 nm (pump resonance discussed in the main text) with extracted Q factors. (d) Near-visible transmission spectrum measured from 776-780 nm (New Focus TLB-6712) and 808.5-809 nm (M2 Sol-sTiS). (e) An under-coupled resonance around 777.9 nm with extracted Q factors. (f) An over-coupled resonance around 809.7 nm (SH resonance discussed throughout the main text) with extracted Q factors.

Figure S2(a) depicts the transmission spectrum of the PPLN microring for a TE-polarized telecom input. The excited cavity modes were determined to be  $TE_{00}$  modes with an extracted group index  $n_g$  of 2.363, which agrees well with the simulated value of 2.367. The extinction ratios of the resonances were observed to increase then decrease while the corresponding loaded Q factors gradually decreased when scanning from short to long wavelengths, indicating a change from under-coupling to over-coupling [2]. Figures S2(b-c) show the respective under-coupled and over-coupled resonances with its measured Q factors.  $Q_L$  is initially extracted by a Lorentzian fit of the resonance.  $Q_0$  and  $Q_c$  are subsequently determined by  $Q_0 = \frac{2Q_L}{1 \pm \sqrt{T_{\min}}}$  and  $\frac{1}{Q_c} = \frac{1}{Q_L} - \frac{1}{Q_0}$ , where  $+$ ( $-$ ) corresponds to the under (over) coupling condition and  $T_{\min}$  represents the normalized on-resonance transmission. In a similar fashion, the transmission spectrum for a TM-polarized near-visible input is shown in Fig. S2(d) while the respective under-coupled and over-coupled resonances are plotted in Figs. S2(e-f) with the corresponding Q factors. The extracted  $Q_0$  is  $\sim 1.8$  million for the telecom TE mode and  $\sim 1.0$  million for the near-visible TM mode. We note

that Figs. S2(c) and (f) respectively depict the pump and SH modes that are specifically discussed in the main text.

## 3. JUSTIFICATION OF QUASI-PHASE MATCHED (AS OPPOSED TO MODAL-PHASE MATCHED) SHG FROM Z-CUT PPLN MICRORINGS

Due to the large second-order nonlinear susceptibility intrinsic to the LN material, it may be a concern that even at a low power, given the right modal-phase matching (MPM) condition, a non-trivial amount of second-harmonic (SH) power can be observed and wrongly attributed to a result of quasi-phase matching (QPM). In this section, we provide ample justification from systematic studies of modal-phase-matched microring widths, theoretical efficiency calculations, as well as experimental results, that the observed SHG under a  $TE_{00}$  pump is in fact due to the QPM instead of MPM between pump  $TE_{00}$  and SH high-order TM modes.



**Fig. S3.** Simulation of the MPM index curves between the fundamental TE mode (solid red line, 1617.4 nm) and high-order SH modes (dashed line, 808.7 nm) in a LN microring with a fixed radius of  $70 \mu\text{m}$  and an etched thickness of  $420 \text{ nm}$  from  $600 \text{ nm}$  (original LNOI thickness). The MPM widths are marked by I, II, III, IV, and V respectively, and are consistent with the labels in Table S1.

**Table S1.** MPM widths simulation with the respective mode profiles, calculated overlap factors and SHG efficiencies

	I	II	III	IV	V
$W_{\text{ring}} (\mu\text{m})$	1.10	1.26	1.47	1.74	2.14
Mode profile					
$\zeta (/ \mu\text{m})$	0.063	0.053	$\sim 0$	$\sim 0$	0.013
$\eta (\%/W)$	63,000	42,000	$\sim 0$	$\sim 0$	2,000

Figure S3 shows the effective refractive indices of the pump fundamental TE mode (red solid line) and high-order SH modes (colored dashed lines) with increasing microring width. The simulation was performed using a finite-difference method (FDM) mode solver (FIMMWAVE, Photon Design, UK). The intersections of the red solid line with colored dashed lines denote the MPM microring widths, which are 1.10, 1.26, 1.47, 1.74,  $2.14 \mu\text{m}$  and marked by I, II, III, IV, and V, respectively. A systematic

study of each MPM width is illustrated in Table S1, including the simulated mode profile, modal overlap factor  $\zeta$ , as well as the calculated SHG efficiency  $\eta$  using the experimentally measured Q factors (Figs. 3(b-c) in the main text). Based on these theoretical results, the highest  $\eta$  occurs when the fundamental TE mode is modal-phase-matched to the near-visible TM<sub>20</sub> mode at a microring width of 1.10  $\mu\text{m}$  (case I in Table S1). Even the highest predicted  $\eta$  ( $\sim 63,000\%/W$ ) via MPM is significantly lower than the experimental  $\eta$  ( $\sim 250,000\%/W$ ) observed from the PPLN microring device due to a much smaller mode overlap. Furthermore, our LN microrings have a fixed width of 1.80  $\mu\text{m}$ , which were specially designed to be far from the optimal MPM width of 1.10  $\mu\text{m}$ . Consequently, no SHG signals were observed from an unpoled microring under a weak TE<sub>00</sub> pump as indicated in Fig. S4(a). Distinct SHG signals were only observed from the same microring after the periodic poling with the same pump and similar Q factors (as shown in Fig. S4(b)), further showing that the efficient frequency doubling in the PPLN microring results from the QPM.

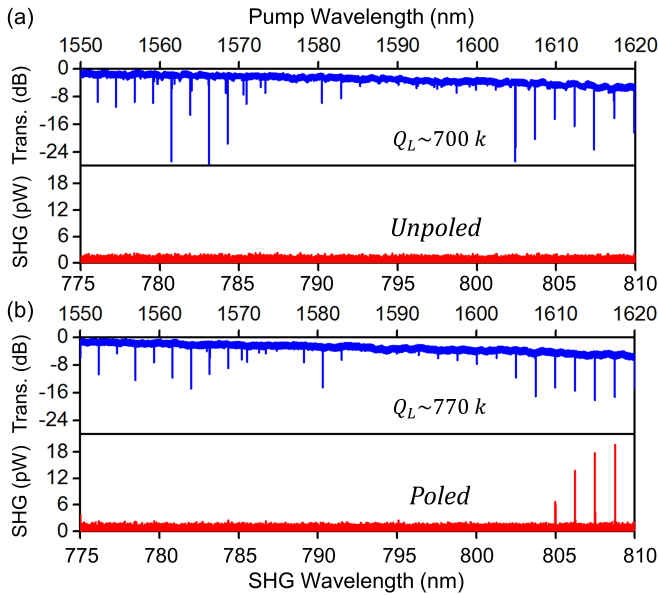


**Fig. S4.** (a) Pump transmission and SHG spectra from an unpoled device. No SHG signals were observed by sweeping a tunable laser across a number of telecom TE<sub>00</sub> modes with an external input power of -13 dBm. (b) Pump transmission and SHG spectra from the same device after poling. Distinct quasi-phase matched SHG peaks are identified.

#### 4. CALIBRATION OF ON-CHIP POWERS AND SHG CONVERSION EFFICIENCY

The calibration method of on-chip pump, SHG powers and conversion efficiency is based on the setup shown in Fig. S5. Several assumptions are made in the calibration process: (1) The fiber-to-chip insertion loss for both sides of the chip are the same, due to the symmetry of the device design, which has been confirmed by the consistent SHG efficiencies when pumping the devices from different sides. (2) Optical propagation losses in the waveguide are small enough to be ignored. (3) The polarization of the input is optimized to be purely TE for the telecom input and TM for the near-visible input. Subsequently, the telecom and near-visible powers are respectively

measured using a calibrated power meter immediately before ( $P_{0,tele/nvis}$ ), after the lensed fibers ( $P_{1,tele/nvis}$ ) and after the off-chip WDM ( $P_{2,tele/nvis}$ ). The fiber-to-chip insertion losses (IL) for pump TE and SH TM modes per facet can be calculated as:  $IL_{tele/nvis} = \sqrt{\frac{P_{1,tele/nvis}}{P_{0,tele/nvis}}}$ . The insertion losses of the off-chip WDM are calculated by  $\frac{P_{2,tele/nvis}}{P_{1,tele/nvis}}$ , which are 0.5 dB and 3.0 dB for the telecom and near-visible light, respectively. Therefore, based on the power measured by the photo-detectors ( $P_{P/SHG,PD}$ ) as shown in Fig. S5, the on-chip pump and SHG powers are calculated as:  $P_{P/SHG} = P_{P/SHG,PD} \times \frac{\sqrt{P_{0,tele/nvis} \times P_{1,tele/nvis}}}{P_{2,tele/nvis}^2}$ . The SHG efficiency  $\eta$  can be finally derived from  $\frac{P_{SHG}}{P_P^2}$ .

Table S2 presents the measured Q factors, calibrated fiber-to-chip insertion losses and SHG efficiencies from four PPLN microring devices. An optimal SHG efficiency  $\eta$  of 250,000%/W was achieved from device 1 as discussed in the main text. Meanwhile, an average  $\eta$  of 175,000%/W with a standard deviation of 45,000%/W was obtained, taking into consideration the variation of the insertion losses, waveguide-microring coupling rates, and intrinsic Q factors during the device design and fabrication process.

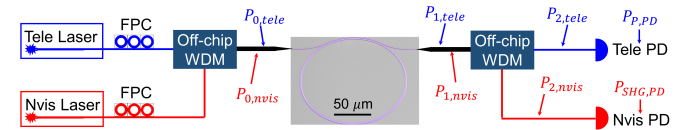


**Fig. S5.** Sketch of the setup to calibrate the on-chip powers and conversion efficiency.

**Table S2. Calibrated SHG efficiency  $\eta$  from multiple devices**

Dev.	$\lambda_{pump}$ (nm)	$Q_{L,tele/nvis}$	$Q_{0,tele/nvis}$	$IL_{tele/nvis}$ (dB/facet)	$\eta$ (%/W)
1	1617	800 k / 180 k	1.8 M / 1.0 M	9.0 / 12.6	250,000
2	1522	690 k / 290 k	1.0 M / 980 k	8.0 / 13.8	130,000
3	1520	1.1 M / 370 k	1.9 M / 590 k	8.8 / 12.5	170,000
4	1518	1.2 M / 480 k	1.5 M / 610 k	8.5 / 13.5	150,000

#### REFERENCES

1. C. L. Sones, S. Mailis, W. S. Brocklesby, R. W. Eason, and J. R. Owen, "Differential etch rates in z-cut LiNbO<sub>3</sub> for variable HF/HNO<sub>3</sub> concentrations," J. Mater. Chem. **12**, 295–298 (2002).
2. Q. Li, M. Davanço, and K. Srinivasan, "Efficient and low-noise single-photon-level frequency conversion interfaces using silicon nanophotonics," Nat. Photonics **10**, 406 EP– (2016).